

A novel approach for unraveling the energy balance of water surfaces with a single depth temperature measurement

Jiachuan Yang,¹ Zhi-Hua Wang,^{1*} Qi Li,² Nikki Vercauteren,³ Elie Bou-Zeid,² Marc B. Parlange⁴

¹School of Sustainable Engineering and the Built Environment, Arizona State University, Tempe, Arizona

²Department of Civil and Environmental Engineering, Princeton University, Princeton, New Jersey

³Department of Mathematics and Computer Science, Freie Universität Berlin, Berlin, Germany

⁴Department of Civil Engineering, The University of British Columbia, Vancouver, Canada

Abstract

The partitioning of solar energy over the Earth's surface drives weather and climate of the coupled land–ocean–atmosphere system. Over water surfaces, the evolution of water temperatures at a given depth in the mixed layer implicitly contains the signature of surface energy partitioning, and as such it can be used to diagnose the surface energy balance. In this study, we develop a novel numerical scheme by combining the Green's function approach and linear stability analysis to estimate the water surface energy balance using water temperature measurement at a single depth. The proposed method is capable of predicting water temperature in the mixed layer, and solving for the components of the surface energy budgets with physically based schemes. Evaluation against in situ measurement and the maximum entropy production method demonstrates that this approach is robust and of good accuracy. It is found that performance of the proposed method depends strongly on the accurate estimation of turbulent thermal diffusivity from in situ measurements, which carries information of meteorological and limnological conditions. Without explicitly using wind speed or temperature/moisture gradient, the proposed approach reduces uncertainty and potential error associated with meteorological measurements in estimation of water surface energy balance.

Partitioning of the solar energy into its various components over the Earth's surface drives the global energy and water cycles. Since water occupies about 71% of the Earth's total surface area, accurate estimation of the surface fluxes over water (including sensible heat and latent heat fluxes to the atmosphere, and heat transported to subsurface thermal mass) is of fundamental importance not only for limnology and oceanography, but also in numerical simulations of regional and global weather and climatic processes. To predict the energy fluxes over a water surface, a number of methods have been developed during recent decades, which can be broadly categorized into two groups. The first group simply uses land surface models in which turbulent heat fluxes are estimated using bulk transfer formulae (Oleson et al. 2010; Best et al. 2011; Niu et al. 2011). The water surface is treated as non-vegetated land surface in the models, and the accuracy of predicted turbulent heat fluxes is largely determined by the parameterization of the transfer coefficient. Existing

parameterization schemes in this group vary in complexity and assumptions, and no single scheme outperforms others under all conditions (Henderson-Sellers et al. 2003). The second group encompasses empirical models derived from regression analysis of in situ measurements (Morton 1983; Granger and Hedstrom 2011). This group of models mainly focuses on prediction of the latent heat flux, and the resulting site-specific relation may not be applicable to water surface under different oceanographic and meteorological conditions. It is noteworthy that the land surface models and empirical models have two limitations in common. First, the estimated heat fluxes are not necessarily constrained by conservation of energy at the water surface. This can lead to a large residual in the surface energy balance, known as the surface energy imbalance closure problem (Leuning et al. 2012). Second, model predictions are strongly affected by multiple meteorological variables, such as wind speed, air temperature, and moisture (Kiehl and Trenberth 1997). Measurement error related to individual variables is amplified and necessarily leads to great uncertainties in the modeled fluxes.

Developed from different perspectives, two recently proposed numerical methods for estimating surface energy budgets have been able to overcome the aforementioned limitations. The

*Correspondence: zhwang@asu.edu

Additional Supporting Information may be found in the online version of this article.

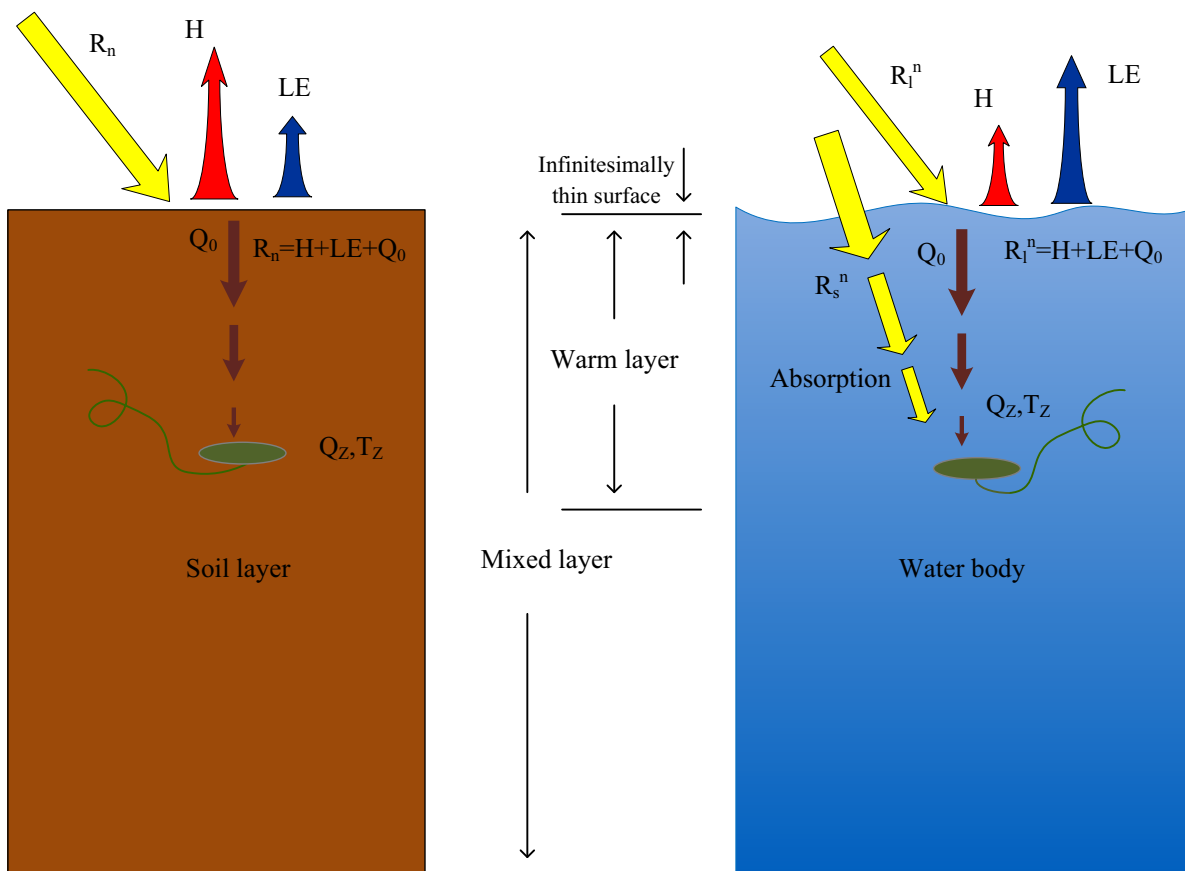


Fig. 1. A schematic for energy balance and heat transfer over water and land surface. R_n is the net radiation; R_s^n and R_l^n denote the net shortwave and longwave radiation; H is the sensible heat flux; LE is the latent heat flux; Q_0 and Q_z are the heat transported to the subsurface thermal mass, at the surface and at depth z , respectively; and T_z is the temperature at depth z . The vertical length of the graph is not in scale.

methods are capable of predicting surface energy budgets without explicitly using temperature and moisture gradients, wind speed, and empirical parameters, while inherently satisfying the conservation of energy at the interface. The first method is based on the maximum entropy production (MEP) principle (Wang et al. 2014), which predicts the surface energy budget as the most probable and macroscopically reproducible distribution that produces the maximum entropy with given information (Dewar 2005; Wang and Bras 2009). Evaluation against in situ measurements verified accuracy of the MEP model over both land and water surfaces (Wang and Bras 2011; Wang et al. 2014). The second method is the numerical procedure developed by Yang and Wang (2014). Using Green’s function approach, the method is able to reconstruct soil thermal field from a single depth soil measurement of either temperature or heat flux (Wang 2012; Wang and Bou-Zeid 2012). Once the heat flux into the subsurface is obtained, the turbulent fluxes into the atmosphere are estimated using linear stability analysis (Yang and Wang 2014). The model’s accuracy and reliability have been assessed using field measurements. Compared with the MEP model, the numerical procedure has better accuracy, especially

for the ground heat flux (Yang and Wang 2014); however, it has not yet been tested over water surfaces.

Compared with land surface, surface energy partitioning over a water surface is further complicated due to the penetration and absorption of solar radiation in the water body. Thermal stratification and turbulent mixing in water bodies are also distinct from subsurface heat transfer process in soils. A schematic comparing surface energy balance over water and land surface is shown in Fig. 1. The goal of this study is thus to generalize the numerical procedure, originally developed for land surface via combined Green’s function approach and linear stability analysis, to estimate the water surface energy balance using temperature measurement at a single depth. The model’s performance is tested against in situ measurement over Lake Geneva, Switzerland. The effects of turbulent heat transfer, radiation penetration and absorption are elucidated by a parametric analysis.

Methodology

Considering an infinitesimally thin layer at the water surface (Fig. 1), and ignoring the shortwave absorption at the

surface since liquid water is mostly transparent to solar radiation, the surface energy balance can be written as:

$$R_1^n = H + LE + Q_0 \quad (1)$$

where R_1^n is the net longwave radiation, H , LE , and Q_0 denote the sensible heat, latent heat, and heat transported to deeper water at the surface, respectively (Q_0 is usually denoted by G_0 over land). Each flux on the right-hand side of Eq. 1 can be considered as a “dissipative” term that consumes energy at the surface and restores the system to “equilibrium.” Shortwave radiation penetrates through the water surface and warms subsurface water layers. Significant warming begins near the surface and heat is propagated into deeper water level driven by turbulent mixing as a result of the surface wind shear. In general, roughly half of the radiative heat is absorbed in the upper 2 m (Fairall et al. 1996). This layer is defined as a warm layer (see Fig. 1) in the upper mixed layer, because its radiation-induced warming is significantly larger than that in the deeper part.

Q_0 and subsurface heat transfer carry the information of surface energy partitioning and conserve it in the mixed layer. Consequently, within the mixed layer, the thermal field in water body can be reconstructed by retrieving the signal from a single depth measurement. Across the thermocline immediately beneath the mixed layer, the surface forcing signal might be lost as heat transfer is strongly affected by deep water temperature. Hence, this study focuses on the mixed layer of water bodies, which ranges from water surface to a depth of 2–13 m over lakes (Fee et al. 1996); but we note that the approach is also applicable over comparable depths even if the water surface is fully quiescent and not mixed (sunny days with weak winds). The one-dimensional heat transfer in the mixed layer is given by:

$$\frac{\partial T(z, t)}{\partial t} = \kappa \frac{\partial^2 T(z, t)}{\partial z^2} + s(z, t) \quad (2)$$

with boundary conditions:

$$-\lambda \frac{\partial T(z, t)}{\partial z} \Big|_{z=0} = f(t), \quad -\lambda \frac{\partial T(z, t)}{\partial z} \Big|_{z=D_m} = 0 \quad (3)$$

and initial condition:

$$T(z, 0) = T_i(z) \quad (4)$$

where $T(z, t)$ is the water temperature at depth z and time t , $\kappa = \lambda / C_w$ the thermal diffusivity (which should include the turbulent mixing where applicable), λ and C_w the thermal conductivity and heat capacity of water, respectively, $s(z, t)$ a source term due to absorption of shortwave solar radiation, $f(t)$ an analytical function prescribing surface flux forcing, D_m the depth of mixed layer, and $T_i(z)$ the initial temperature profile. Compared with heat transfer over land surface (Yang and Wang 2014), absorption of shortwave solar

radiation adds the heating source term $s(z, t)$ to Eq. 2 and creates additional complexity for reconstruction of water thermal fields (see Fig. 1). One underlying assumption of Eq. 2 is that κ does not change significantly with depths, thus the proposed method requires a relatively constant thermal diffusivity in the study depths of water body. Furthermore, thermal diffusivity is enhanced through turbulent mixing in the water (Wüest and Lorke 2003). This will be discussed further in the following section.

Using a Green’s function approach for the canonical heat conduction problem in a finite field, the general solution for temperature resulting from Eqs. 2 to 4 is (Cole et al. 2010):

$$\begin{aligned} T(z, t) = & \int_{z'=0}^{D_m} g(z, t|z', 0) T_i(z') dz' + \int_{\tau=0}^t \\ & d\tau \int_{z'=0}^{D_m} g(z, t|z', \tau) s(z', \tau) dz' \\ & + \int_{\tau=0}^t \frac{\kappa}{\lambda} f(\tau) g(z, t|z', \tau) d\tau \end{aligned} \quad (5)$$

where z' and τ are integration variables, $g(z, t|z', \tau)$ is the impulse Green’s function solution corresponding to an influx of heat with unity strength (mathematically represented as a Dirac delta function at the surface):

$$g(z, t|z', \tau) = \frac{1}{\sqrt{4\pi\kappa(t-\tau)}} \left[e^{-(z-z')^2/4\kappa(t-\tau)} + e^{-(z+z')^2/4\kappa(t-\tau)} \right] \quad (6)$$

On the right-hand side of Eq. 5, the first, second, and third terms represent the contribution of the initial conditions, source term, and boundary conditions to the temperature variability, respectively. Combination of the first and third terms represents a homogeneous heat conduction problem over land surface, whose solution is given by Wang and Bou-Zeid (2012):

$$\begin{aligned} & \int_{z'=0}^{D_m} g(z, t|z', 0) T_i(z') dz' \\ & + \int_{\tau=0}^t \frac{\kappa}{\lambda} f(\tau) g(z, t|z', \tau) d\tau = T_i(z) \\ & + \int_0^t f(t-\tau) dh(z, \tau) \end{aligned} \quad (7)$$

where $h(z, \tau)$ is the step Green’s function solution, which resolves the singularity of the impulse Green’s function by temporal integrations (Wang et al. 2005):

$$h(z, \tau) = \frac{\kappa}{\lambda} \int_{\tau=0}^t g(z, \tau) d\tau = \frac{2\sqrt{\kappa\tau/\pi}}{\lambda} \exp\left(-\frac{z^2}{4\kappa\tau}\right) - \frac{z}{\lambda} \operatorname{erfc}\left(\frac{z}{2\sqrt{\kappa\tau}}\right) \quad (8)$$

Therefore, the major outstanding challenge is to solve the contribution of source term $s(z, t)$ to the solution of water temperature. According to the Beer–Lambert law (Jerlov 1976), the intensity of solar radiation decreases

Table 1. Summary of absorption coefficients and radiation fractions for different portions of the solar spectrum in water (Paulson and Simpson 1981).

Wavelength portion of the spectrum (10 ⁻⁶ m)	Absorption coefficient, μ (m ⁻¹)	Fraction of radiation, η
0.2–0.6	2.874×10^{-2}	0.2370
0.6–0.9	4.405×10^{-1}	0.3600
0.9–1.2	3.175×10^1	0.1790
1.2–1.5	1.825×10^2	0.0870
1.5–1.8	1.201×10^3	0.0800
1.8–2.1	7.937×10^3	0.0246
2.1–2.4	3.195×10^3	0.0250
2.4–2.7	1.279×10^4	0.0070
2.7–3.0	6.944×10^4	0.0004

exponentially as sunlight travels through the water, leading to the following source term due to absorption at a given depth z :

$$s(z, t) = \frac{R_s^n(t)}{C_w} \sum_j \eta_j \mu_j e^{-\mu_j z} \quad (9)$$

where R_s^n is the net shortwave radiation at the water surface, μ_j and η_j denote the absorption coefficient and fraction of radiation of the j th spectral component. Note in Eq. 9, the continuous spectrum is divided into limited number of bands and represented using a finite summation. Defant (1961) reported the optical properties of seawater based on experimental studies and identified coefficients for 9 bands, which have been adopted in later studies for various water surfaces (Paulson and Simpson 1981; Wang et al. 2014). The 9-band approximation is used in this study, with all parameters summarized in Table 1. The absorption coefficients also depend on water characteristics; and properties such as turbidity, organic matters, and vegetation can significantly modify the attenuation of solar radiation in the water (Jerlov 1976; Paulson and Simpson 1981). Substituting Eqs. 6 and 9 into Eq. 5 yields (see Supplementary Materials for a detailed derivation):

$$\int_{\tau=0}^t d\tau \int_{z'=0}^{D_m} g(z, t|z', \tau) s(z', \tau) dz' = \int_{\tau=0}^t \sum_j \frac{R_s^n(t-\tau) \eta_j \mu_j}{C_w} dA_j(z, \tau) \quad (10)$$

where:

$$A_j(z, \tau) = \frac{e^{\kappa\tau\mu_j^2 - \mu_j z}}{2\kappa\mu_j^2} \operatorname{erfc}\left(\frac{2\kappa\tau\mu_j - z}{\sqrt{4\kappa\tau}}\right) + \frac{e^{\kappa\tau\mu_j^2 + \mu_j z}}{2\kappa\mu_j^2} \operatorname{erfc}\left(\frac{2\kappa\tau\mu_j + z}{\sqrt{4\kappa\tau}}\right) + \frac{z}{\kappa\mu_j} \operatorname{erf}\left(\frac{z}{\sqrt{4\kappa\tau}}\right) + \sqrt{\frac{4\tau}{\kappa\pi\mu_j^2}} e^{-z^2/4\kappa\tau} \quad (11)$$

In Eq. 7, the boundary condition at the surface yields $f(t) \equiv Q_0(t) + R_s^n(t)$. Therefore the solution of water temperature at any depth is given by:

$$T(z, t) = T_i(z) + \int_0^t [Q_0(t-\tau) + R_s^n(t-\tau)] dh(z, \tau) + \int_{\tau=0}^t \sum_j \frac{R_s^n(t-\tau) \eta_j \mu_j}{C_w} dA_j(z, \tau) \quad (12)$$

A numerical quadrature is needed here to discretize the integrand for explicitly formulating the surface temperature T_s (which is taken here as the temperature of the top few millimeters in water) in terms of water temperature at an arbitrary depth. Discretizing the time continuum into $\{t = t_k | k = 0, 1, 2, \dots, n\}$ where n is the number of time steps, and applying the trapezoidal rule to Eq. 12, we obtain:

$$Q_0(n) = \left\{ 2\bar{T}(z, n) - J_{n-1}(Q_0, \Delta h_z) - J_n(R_s^n, \Delta h_z) - \sum_j \frac{\eta_j \mu_j}{C_w} \sum_{k=1}^{n-1} [R_s^n(n-k+1) + R_s^n(n-k)] \Delta A_j(z, k) \right\} \frac{1}{\Delta h_z(1)} \quad (13)$$

where:

$$J_{n-1}(Q_0, \Delta h_z) = Q_0(n-1) \Delta h_z(1) + \sum_{k=2}^{n-1} [Q_0(n-k+1) + Q_0(n-k)] \Delta h_z(k) \quad (14)$$

$$J_n(R_s^n, \Delta h_z) = \sum_{k=2}^n [R_s^n(n-k+1) + R_s^n(n-k)] \Delta h_z(k) \quad (15)$$

where $\bar{T}(z, n) = T(z, n) - T_i(z)$ is a normalized temperature, $\Delta h_z(k) = h_z(t_k) - h_z(t_{k-1})$, and $\Delta A_j(z, k) = A_j(z, t_k) - A_j(z, t_{k-1})$. It is clear from Eq. 13 that $Q_0(t)$ can be obtained from known quantities, including time series of $Q_0(t' < t)$ (prior to the current time step), measured time series of water temperature $T(z, t)$, and net shortwave radiation at the water surface $R_s^n(t)$. Once the time series of $Q_0(t)$ is estimated, water temperature at any depth can be obtained by substituting $Q_0(t)$ into Eq. 12 with prescribed water depth. Similarly, the Green's function approach enables reconstructing time series of Q at any depth from a single depth measurement of $Q(z, t)$ in the mixed layer (Wang 2012).

After time series of Q_0 and T_s are obtained, the sensible and latent heat fluxes can be estimated via linear stability analysis. Linear stability analysis estimates turbulent heat fluxes by quantifying their relative efficiencies in restoring the thermodynamic equilibrium of surface energy balance when a perturbation is imposed (Bateni and Entekhabi 2012). Detailed information of the method can be found in previous studies (Bateni and Entekhabi 2012; Yang and Wang 2014). Using linear stability analysis, the relative efficiency of LE to H for a saturated surface in the absence of advective effects in the atmosphere, i.e. when air near the

water surface is in equilibrium with that surface, is given by Yang et al. (2013):

$$\Delta_{re} = \frac{LE}{H} = \frac{L_v}{c_p} \left(\frac{\partial q_s^*}{\partial T} \right) \Big|_{T=T_s} \quad (16)$$

where c_p is the specific heat of air; L_v is the latent heat of vaporization for water; q_s^* is the saturated specific humidity. Using the Clausius–Clapeyron equation, q_s^* is a function of surface temperature and therefore Δ_{re} depends only on T_s . Detailed derivation of Δ_{re} is provided in Yang and Wang (2014). The sensible and latent heat flux are then given by:

$$H = \frac{R_l^n - Q_0(n)}{\Delta_{re} + 1}, \quad LE = \frac{\Delta_{re}}{\Delta_{re} + 1} [R_l^n - Q_0(n)] \quad (17)$$

It is clear from Eqs. 13 and 17 that the proposed method only requires the surface radiation budget and water temperature at a single depth as input. The water surface fluxes are formulated without explicitly using meteorological variables such as wind speed, air temperature, and humidity. This reduces the error and uncertainty of the modeled surface fluxes since the measurement error of radiation budget and temperature are significantly smaller than that of wind speed and temperature/moisture gradient (Wang et al. 2014). Furthermore, the model prediction of the fluxes is bounded by the conservation of energy at the surface. The model however requires equilibrium between the air and water layers near the interface (weak horizontal heat transfer in both layers); turbulent fluxes are computed at a rate dissipating radiative energy to maintain that surface equilibrium.

In a nutshell, the numerical method for estimating the water surface energy balance developed in this study follows a two-step procedure. First, heat transported to deeper water at the surface Q_0 is estimated by solving one-dimensional heat transfer problem via Green's function approach. Using Eqs. 2-4 for heat transfer in the mixed layer, the method assumes that lateral boundary conditions and horizontal heat transport play a negligible role in determining water temperatures. Hence, the developed method is preferably applicable for large water bodies with homogeneous or weak horizontal heat transport, and far from water–land boundaries. Estimating Q_0 in moving water bodies with complex lateral boundaries (e.g., rivers) will require adding a horizontal heat source term on the right-hand side of Eq. 2 as well as a reasonable description of the lateral boundary conditions. Moreover, turbulent fluxes H and LE are predicted based on the Q_0 estimated in the first step and the measured net longwave radiation R_l^n .

The major underlying assumptions of the proposed method include: (1) the quasi-static thermal equilibrium between the water surface and near-surface atmosphere, inherited from the premise of the linear stability analysis (Bateni and Entekhabi 2012), and (2) the analogy in turbulent heat and moisture transport (Yang and Wang 2014). Approaching the

thermal equilibrium, the evolution of the state of near-surface air (i.e., temperature, humidity, etc.) follows closely that of the surface (Bateni and Entekhabi 2012) with its signal embedded in the evolution of water surface state. In addition, the analogy in transport mechanism of heat and moisture is commonly assumed in the literature when in situ measurements are unavailable (Liang et al. 1994; Mote and O'Neill 2000), canceling the dependence of the LE/H ratio on the aerodynamic resistance. Subsequently, H and LE can be formulated without explicitly using meteorological variables based on these assumptions. Using flux measurements over the ocean, Large and Pond (1982) found that transfer coefficients of moisture and heat are very similar under various meteorological conditions as long as the atmospheric layer is unstable. However, the assumptions do not necessarily hold all the time (Stensrud 2009). For instance, the transfer coefficient of heat is found to be significantly smaller than that of moisture in a stable air layer (Large and Pond 1982). Wallace and Hobbs (2006) showed that the magnitude of transfer coefficients of moisture and heat diverges as wind speed increases. Strong horizontal air movement can also break the equilibrium between water surface and near-surface air. Therefore, better accuracy of the current method is expected in predicting surface turbulent heat fluxes when applied to unstable atmospheric conditions with low wind speeds.

Site description

In this study, the proposed method is tested against in situ measurements over Lake Geneva, Switzerland. The field data were collected during the Lake-Atmosphere Turbulent Exchange (LATEX) field campaign from 15 August to 27 October 2006. The experimental platform was located about 100 m offshore in a shallow part of the lake without significant aquatic vegetation (Vercauteren et al. 2008). Meteorological variables such as wind velocity, air temperature, and humidity were measured at four different heights above the water surface using a vertical array of sensors. In this study, we used the measurements at 1.66 m for subsequent analysis, which is the closest to the water surface. A water temperature profile was measured at a frequency of 5 min using a Raman-scattering fiber-optic temperature profiler. About 1 m of the profiler was above the water surface, whereas the remaining 1.85 m was submerged in water. The vertical and temperature resolution of the profile is 0.004 m and 0.01°C. Due to technical issues, several gaps exist during the measurement period. Detailed information on equipment and experimental setup can be found in Vercauteren et al. (2008, 2011).

Results and discussion

Sensitivity analysis

Penetration and absorption of shortwave radiation are the major players that distinguish surface energy partitioning

and subsurface heat transfer for water bodies from their land counterparts. From Eq. 9, it is clear that radiative absorption is mainly affected by the available net shortwave radiation at the water surface $R_s^n(t)$ and the absorption coefficient μ . For the study site, Vercauteren et al. (2011) found that the effective thermal diffusivity in top 1.5 m of the lake mainly depended on turbulence, and hence was much larger here than molecular diffusivity. By analyzing phase shift and amplitude of variation of water temperature, they estimated an effective thermal diffusivity ranging from 6.6×10^{-5} to $3.0 \times 10^{-3} \text{ m}^2 \text{ s}^{-1}$ in sunny conditions with low wind speeds. Thermal diffusivity determines the heat transfer rate in water and has a significant effect on the temperature solution. Thus, we conducted a parametric analysis to quantify the sensitivity of water temperature to $R_s^n(t)$, μ and κ . The simulation starts at 00:00 and ends at 24:00 on 4 September 2006, a sunny day with low wind speeds. As shown in Eqs. 12 and 13, constructing the subsurface thermal field requires $R_s^n(t)$ and temperature measurement at a single depth as input. Here, the measured water surface temperature from the fiber-optic temperature profiler is used. To simplify the problem in the parametric analysis, a uniform initial temperature profile is assumed, and net shortwave radiation at the water surface is prescribed by a sinusoidal function:

$$R_s^n = A \sin(\omega t_{\text{loc}} + \phi), \quad 6 \leq t_{\text{loc}} \leq 18 \quad (18)$$

where A is the amplitude of diurnal variation, $\omega = 2\pi/24 \text{ rad h}^{-1}$ is the angular speed of rotation of the earth, t_{loc} is the local time in hours, ϕ is the phase lag. Three sets of simulations were carried out separately to illustrate the impact of $R_s^n(t)$, μ , and κ on the vertical profile of water temperature. Four different amplitudes were tested in the first set, namely, 0, 200, 400, and 600 W m^{-2} , while μ is adopted from Table 1 and a mean thermal diffusivity of $1.0 \times 10^{-4} \text{ m}^2 \text{ s}^{-1}$ is used for κ . For the second set, μ is multiplied by a parameter α to represent the absorption process with different water characteristics. Tested α ranges from 0.5 to 4, and the amplitude A and thermal diffusivity κ have a constant value of 400 W m^{-2} and $1.0 \times 10^{-4} \text{ m}^2 \text{ s}^{-1}$, respectively, in these runs. In the last set, κ is varied between 1×10^{-6} and $1 \times 10^{-3} \text{ m}^2 \text{ s}^{-1}$, while μ is adopted from Table 1 and A is fixed to 400 W m^{-2} .

Vertical profiles of predicted water temperature with varying A at 12:00 and 16:00 are shown in Fig. 2a,b. Without shortwave radiation absorption, heat transfer over the water surface is identical to that over the land surface. The profile with $A=0$ represents the temperature solution driven by homogeneous heat conduction, where the surface forcing is embedded in the time series of surface temperature. As net longwave radiation at the surface is the sole energy source, water temperature decreases with depth. When there is shortwave radiation absorption, it provides additional energy other than surface forcing that heats up water unevenly in

the vertical direction, which modifies the homogeneous heat transfer process in the water body. The difference between various temperature profiles in Fig. 2a,b thus represents the cumulative effect of heat transfer and radiation absorption at different times. Fig. 2a,b clearly show that the water temperature increases with the intensity of shortwave radiation, as expected. At 12:00, the maximum temperature increase is found at the depth of 0.5 m. Compared with the case with no shortwave radiation, temperature increase is about 0.28, 0.55, and 0.83°C for $A = 200, 400,$ and 600 W m^{-2} , respectively. The vertical distribution of temperature increase has a linear relationship with the magnitude of $R_s^n(t)$, as indicated in Eq. 12. Note that with a stronger shortwave radiation, water temperature at a few centimeters depth can be slightly greater than the surface temperature, owing to the large absorption coefficient at the longer end of the solar wavelength band, as presented in Table 1. At 16:00, the maximum temperature (compared with the no radiation case) increase occurred at the depth of 0.9 m. The shift of depth where the maximum temperature increase occurs is due to reduced R_s^n after noontime. The effect of radiation absorption decreases with reduced R_s^n as heat transfer plays a more important role in determining water temperature. As the temperature closer to the surface is consistently higher with decreased radiation intensity, diffusion tends to transfer the large amount of accumulated surface thermal energy to deeper water. At the depth of 1.5 m, shortwave radiation of 600 W m^{-2} will lead to a temperature increase of about 0.51°C at 12:00 and about 0.72°C at 16:00.

Results with different α values at 12:00 and 16:00 are plotted in Fig. 2c,d. By changing α , the vertical absorption of shortwave radiation in the water body is modified, leading to a different vertical distribution of temperature. However, it is clear from Fig. 2c,d that the temperature profiles are insensitive to the selected α values. At 12:00 and 16:00, the maximum temperature difference is less than 0.1°C when α is increased from 0.5 to 4. The negligible impact is caused by the efficiency of turbulence in transferring energy in the mixed layer, which redistributes (mixes) the local effect of modified radiation absorption rapidly. This is a useful result since it indicates that our model skill as assessed in the following section is minimally sensitive to μ , which is a parameter that can vary across sites and with water conditions as explained before (except potentially in sites with very high turbidity).

The impact of κ on water temperature solutions at 12:00 and 16:00 is demonstrated in Fig. 2e,f. It is shown that the vertical distribution of water temperature changes markedly with the magnitude of thermal diffusivity κ . With a small κ value of $1 \times 10^{-6} \text{ m}^2 \text{ s}^{-1}$, heat transfer in the water is so slow that absorption of shortwave radiation essentially dictates the profile. At 12:00, the maximum temperature is found at the depth of 0.05 m, and temperatures deeper than 0.6 m remain mostly unperturbed (warming $<0.2^\circ\text{C}$ as

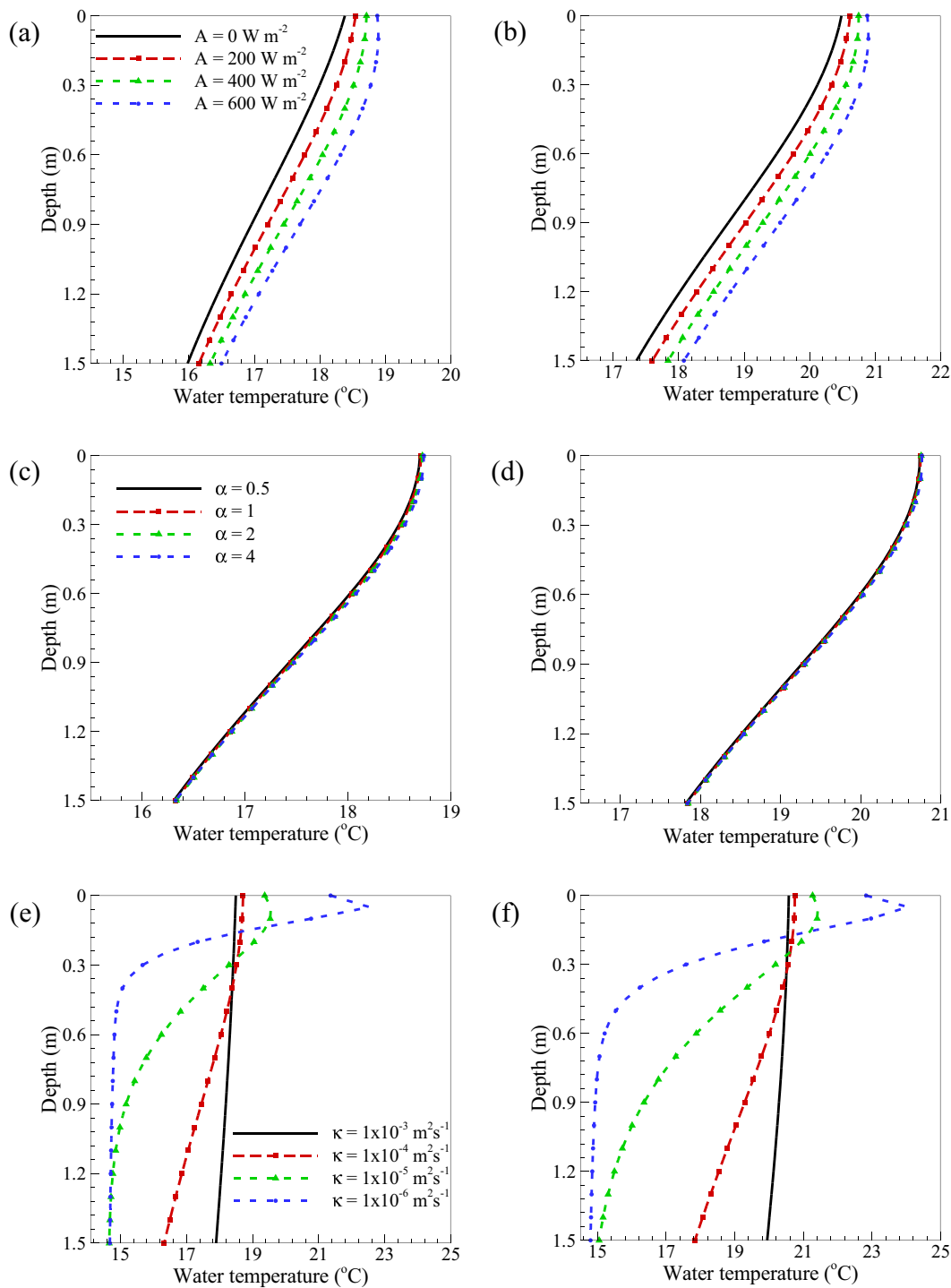


Fig. 2. Vertical profile of predicted water temperature with (a) varying A at 12:00, (b) varying A at 16:00, (c) varying α at 12:00, (d) varying α at 16:00, (e) varying κ at 12:00, and (f) varying κ at 16:00, on 4 September. Reference values of parameters, unless varied and specified in the graph, are $A = 400 \text{ W m}^{-2}$, $\alpha = 1$, $\kappa = 1.0 \times 10^{-4} \text{ m}^2 \text{ s}^{-1}$.

compared with initial temperature). Results constructed from $T_{0.10}$ were very close to results shown in the manuscript. A larger κ value represents a faster heat transfer in the water

body, and therefore tends to smooth the vertical temperature profile. When κ is $1 \times 10^{-3} \text{ m}^2 \text{ s}^{-1}$, large thermal diffusivity transports heat very efficiently, such that absorbed

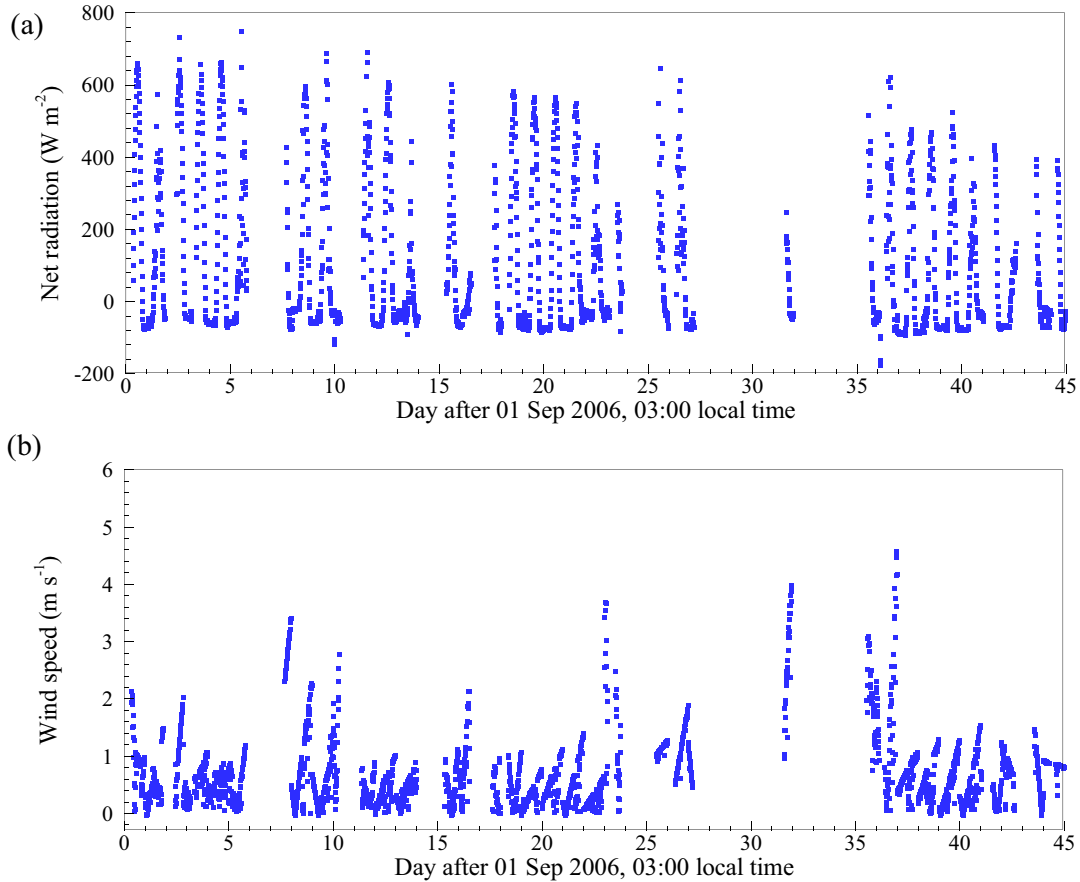


Fig. 3. Measured (a) net radiation and (b) wind speed during the study period from 1 September to 17 October 2006.

energy is redistributed evenly throughout the simulated depths. At 12:00, the difference between surface temperature and water temperature at a depth of 1.5 m is only about 0.6°C. Temperature profiles with different κ values at 16:00 are qualitatively similar to those at 12:00. After 4 hours of heat transfer, under the condition of small thermal diffusivity ($\kappa = 1 \times 10^{-6} \text{ m}^2 \text{ s}^{-1}$), the depth exceeds which water temperature remains mostly uninterrupted (warming $< 0.2^\circ\text{C}$ as compared with initial temperature) shifts from 0.6 m to 0.9 m. The parametric analysis indicates that intensity of the net shortwave radiation $R_s^d(t)$ and thermal diffusivity κ determine the distribution of temperature increase, while the absorption coefficient μ has a negligible impact under a turbulent heat transfer regime.

Reconstruction of water temperature

Following the previous study (Yang and Wang 2014), temperature measurement at 0.05 m depth from fiber-optic temperature profiler is adopted to construct the water thermal field. The simulation period is from 1 September to 17 October 2006. The depth of 0.05 m is selected for the following reasons: (1) it is in the thermally active shallow water layer such that the surface energy balance signal is not

significantly contaminated by numerical errors and instabilities in thermal reconstruction; and (2) it is not too close to the surface such that the signal is not largely influenced by the oscillation of water surface conditions (e.g., waves). Nevertheless, we performed the reconstruction using a depth of 0.1 m and the results were very similar to the ones we report; the reconstruction is thus not very sensitive to the exact depth of the measurements. Measured net radiation and wind speed during the study period are shown in Fig. 3. It is clear from the graph that the lake is under sunny condition with low wind speeds in general. Vercauteren et al. (2008) reported that the heights of the waves in the lake had a median of about 0.03 m and rarely exceeded 0.2 m for wind speeds between 1 and 10 m s^{-1} .

Vertical mixing in the mixed layer is mainly caused by wind stress on the water surface such that κ is not expected to be constant in time and space. By analyzing phase shift and amplitude of variation of water temperature in the lake, Vercauteren et al. (2011) found that high wind speed tends to increase depth of the mixed layer, as it generates stronger shear force at the surface. During September, it was observed that the top 1 m of the lake is generally well mixed with an estimated κ of about $1.2 \times 10^{-4} \text{ m}^2 \text{ s}^{-1}$. Hence, we used a

constant κ of $1.2 \times 10^{-4} \text{ m}^2 \text{ s}^{-1}$ for reconstructing water temperatures in top 1 m of the lake. It is noteworthy that our approach is capable of reconstructing water temperatures with varied κ , as long as temporal variation of κ is available. The diffusivity estimated from field measurements implicitly contains information of mean atmospheric conditions and water column stability in this period. Thus the proposed method here is not entirely uncoupled from atmospheric conditions.

Reconstructing water temperature requires measured net shortwave radiation as input, while only net radiation is available for this particular dataset. To estimate the net shortwave radiation, the Stefan-Boltzmann law is used:

$$R_s^n = R_n - R_l^n = R_n - (\varepsilon_a T_a^4 - \varepsilon_w T_s^4) \quad (19)$$

where ε_a and ε_w denote the emissivity of air and water; σ is the Stefan-Boltzmann constant $5.67 \times 10^{-8} \text{ W m}^{-2} \text{ K}^{-4}$, and T_a is the air temperature in Kelvin. The emissivity of water ε_w is relatively constant; here we used a value of 0.98 following a previous study (Rees and James 1992). The atmospheric emissivity ε_a in Eq. 19 represents the whole atmospheric column of air above the site; it is thus sensitive to various meteorological variables, including air temperature, relative humidity, cloudiness, etc. (Crawford and Duchon 1999), and ranges from the clear-sky value to the fully cloudy value of unity. Following a previous study (Satterlund 1979), ε_a is calculated using:

$$\varepsilon_a = \text{clf} + (1 - \text{clf}) \times \left\{ 1.08 \left[1 - \exp \left(-e_0^{T_a/2016} \right) \right] \right\} \quad (20)$$

where clf is the cloud fraction, e_0 is the vapor pressure in millibar. A clear-sky condition is assumed in this study as cloud fraction cannot be estimated without direct measurement of downward shortwave radiation. Estimated ε_a from the Eq. 20 falls in a small range of 0.84–0.88 for the simulation period over the study site. Considering the air temperature range of 10–20°C during the study period, maximum error in estimated R_s^n and R_l^n is about 51.0–58.5 W m^{-2} . In addition, in the previous section, the sensitivity analysis showed that a difference of 200 W m^{-2} in magnitude of R_s^n leads to a difference of about 0.28°C for water temperatures in the top 1.5 m. Therefore, the error due to ε_a estimation is tolerable for the purpose of water temperature reconstruction in this study.

The air temperature measured at 1.66 m above the water surface is used for Eq. 19 as it is the closest to the surface. Three sets of surface temperature data are available, collected by thermocouple, IR sensor, and fiber-optic temperature profiler, respectively. Measurement from fiber-optic temperature profiler is selected, as it has the highest data availability and is consistent with the input temperature measurement. As water level varies with wind condition throughout the day, surface temperature is determined by finding the sharp

change around still water level in the temperature profile, where difference between two adjacent temperature measurements exceeds 2.5 times of the standard deviation of water temperature.

Comparisons of model predicted surface temperature (T_s), water temperature at 0.15 m ($T_{0.15}$), and water temperature at 1.0 m ($T_{1.0}$) against field observations are shown in Fig. 4. Due to gaps in measured input variables, predicted T_s , $T_{0.15}$ and $T_{1.0}$ are discontinuous. The agreement between prediction and observation is generally good throughout the simulation period, confirming the model's capability in accurately reconstructing water temperature from measurements at another depth in the mixed layer. For $T_{0.15}$ and $T_{1.0}$, the coefficient of determination R^2 is 0.98 and 0.96, and root mean square error (RMSE) is less than 0.1°C, indicating a reasonable goodness-of-fit between predictions and observations. It is found that the model's accuracy of water surface temperature prediction is slightly impaired, as compared with the prediction of water temperature at 0.15 m and 1.0 m. This could be related to the variability of boundary conditions at the water–air interface, e.g., wave, wind shear, boat wakes, etc. Furthermore, Vercauteren et al. (2009) reported that a considerable deviation existed between surface temperature measurements from different sensors. Evaluating the predictions of surface temperature thus becomes challenging with the significant uncertainty and error related to in situ measurements.

In addition, it is also important to evaluate the performance of the method in predicting spatial distribution of water temperature. Simulated water temperature profiles are compared against field measurements in the lake for two days with distinct meteorological conditions: a calm clear day (maximum wind speed $< 1 \text{ m s}^{-1}$), September 20 (Fig. 5a), and a windy day (maximum wind speed $> 5 \text{ m s}^{-1}$), October 8 (Fig. 5b). Though it is aforementioned that the proposed method is preferably applicable for low wind conditions, Fig. 5 shows that reconstructed temperature profiles agree with measurements reasonably well for the sunny day and the windy day. Note that the initial time of simulation for the sunny day and the windy day is 10:00, September 17 and 06:00, October 6, respectively. A full diurnal cycle (warming and cooling of water temperatures) has been simulated before the predicted temperature profiles shown in Fig. 5 to reduce the impact of initial conditions. We should emphasize here that the information of mean atmospheric and water conditions, rather than atmospheric and water variability, is implicitly contained in the estimated diffusivity from field measurements. Thus, it does not contradict the reasonable agreement in Fig. 5 with a same κ for two distinct meteorological conditions. At depths between 0.1 and 1.0 m, difference between predicted and observed water temperatures is less than 0.2°C. The largest deviation of more than 2°C is observed at the surface, which is mainly attributable to measurement errors and fluctuation of boundary

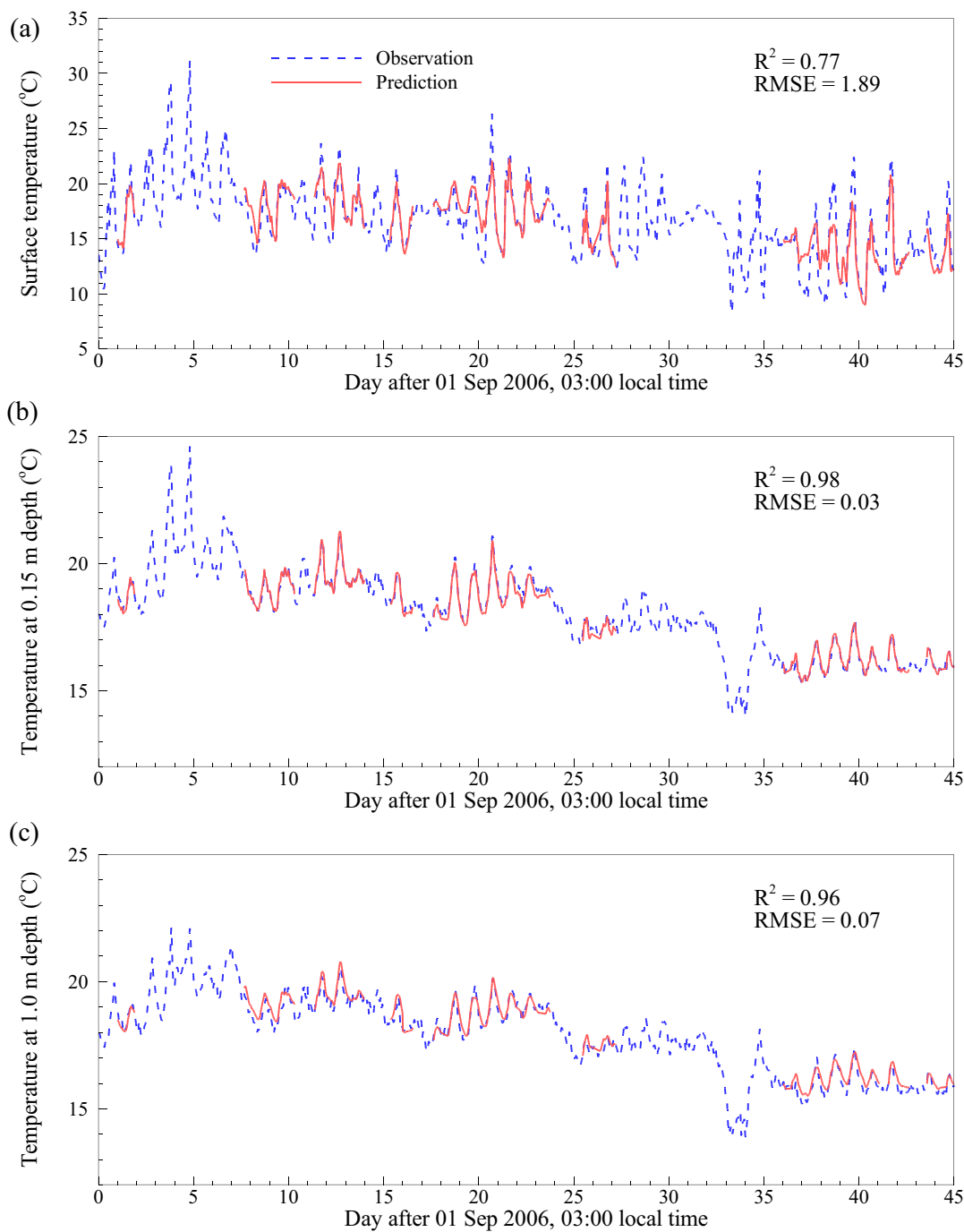


Fig. 4. Comparison of predicted and observed (a) T_s , (b) $T_{0.15}$, and (c) $T_{1.0}$ for 1 September–17 October 2006 (water temperatures reconstructed from $T_{0.05}$).

conditions at the water–air interface. In the vertical direction, surface temperature is the highest (compared with other depths) during daytime (12:00 and 16:00) and the lowest at night (4:00 and 20:00) on the calm clear day. On the other hand, the surface is consistently the coolest point of the profile throughout the diurnal cycle on the windy day. This indicates that presence of solar radiation has a significant

warming effect on water layer close to the surface (<0.1 m) only under a low wind condition.

Prediction of surface energy balance

After the time series of surface temperature is reconstructed, H and LE can be estimated from Eq. 17. Throughout the simulation period, both observed and predicted

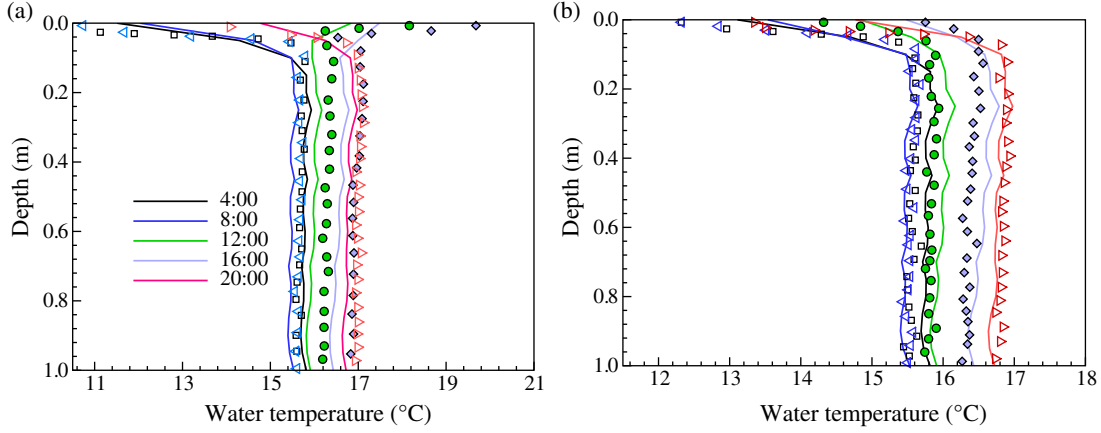


Fig. 5. Evolution of predicted and observed water temperature profiles in the top 1 m of the lake for (a) a calm clear day, September 20, and (b) a windy day, October 8. The solid lines represent model results, while the point markers are for the measurements. Predicted water temperatures are reconstructed from $T_{0.05}$.

turbulent heat fluxes contain several big gaps due to limited data availability. Hence scatter plots are used to compare model prediction against observation over the entire simulation period. Note that due to complexities at the water–air interface, direct in situ measurement of Q_0 at the water surface is extremely challenging. In practice, the most commonly used (hereafter referred to as “the conventional”) approach to estimate Q_0 is through a combination of gradient method and calorimetry (Liebethal et al. 2005):

$$Q_0(t) = -\lambda \left. \frac{\partial T}{\partial z} \right|_{z_q} + \int_0^{z_q} C_w \frac{\partial T}{\partial t} dz - \int_0^{z_q} C_{ws}(z, t) dz \quad (21)$$

where z_q is an arbitrary depth close to surface and equals to 0.05 m in this study. This approach accounts for the vertical gradient of temperature measured at z_q and includes the heat storage in the water body above when determining Q_0 . From Eq. 21 it is clear that the conventional approach uses measured time series of water temperature profiles to calculate Q_0 , while the proposed method in this study (Eq. 13) only requires measured time series of water temperature at a single depth.

Figure 6 shows that predicted Q_0 from the single-depth method in this study agrees well with that from the conventional approach, while modeled turbulent heat fluxes are not highly accurate. RMSEs for H , LE , and Q_0 are about 30, 71, and 22 $W m^{-2}$, respectively. As the model capacity in estimating Q_0 is validated by Fig. 6c, the substantial discrepancy in H and LE is hypothesized as primarily due to the inadequacy of radiation parameterization. The estimate of net longwave radiation entails among other uncertainty in the surface temperature measurement, and its maximum error can be greater than 50 $W m^{-2}$ as illustrated in the previous discussion. The error is propagated to the available energy for turbulent heat fluxes (i.e., $R_1^n - Q_0(n)$ in Eq. 17 equals to measured R_n minus estimated R_1^n from Eqs. 19 and 20),

which can cause a sizable deviation considering the magnitude of H and LE . To verify this hypothesis, we force the available energy for turbulent heat fluxes by explicitly imposing the surface energy balance constraint (i.e., $R_1^n - Q_0(n)$ in Eq. 17 equals to observed $(H + LE)$). A similar treatment was adopted by Vercauteren et al. (2009) to estimate the evaporation arising from the water surface, and is hereinafter referred to as the repartitioning approach. As shown in Fig. 6, with the repartitioning of the available energy using measured dataset, the accuracy of the linear stability analysis method (Eq. 17) is significantly improved and the method is now capable of accurately predicting both sensible and latent heat arising from the lake surface. Values of RMSE for H and LE using the repartitioning approach are 19 and 26 $W m^{-2}$, significantly smaller than those using the estimated radiation (Eq. 19). Nevertheless, it is found that the repartitioning method slightly overestimates H and underestimates LE . This deviation results from the deviation in surface temperature prediction, which is strongly affected by the oscillation of water surface conditions.

Comparison to the MEP model

To illustrate the performance of the method proposed in this study with respect to existing numerical approaches, here we compare it with the MEP model. Wang et al. (2014) recently extended the MEP model for surface energy budgets over water, snow, and ice surfaces. Model prediction shows encouraging agreement with observation from several field experiments. The relative efficiency of LE to H in the MEP model is given by Wang et al. (2014):

$$\Delta_{re} = \frac{LE}{H} = 6 \left(\sqrt{1 + \frac{11 L_v}{36 C_p} \left(\frac{\partial q_s^*}{\partial T} \right)_{T=T_s}} - 1 \right) \quad (22)$$

and Q_0 is calculated by a physically based analytical solution:

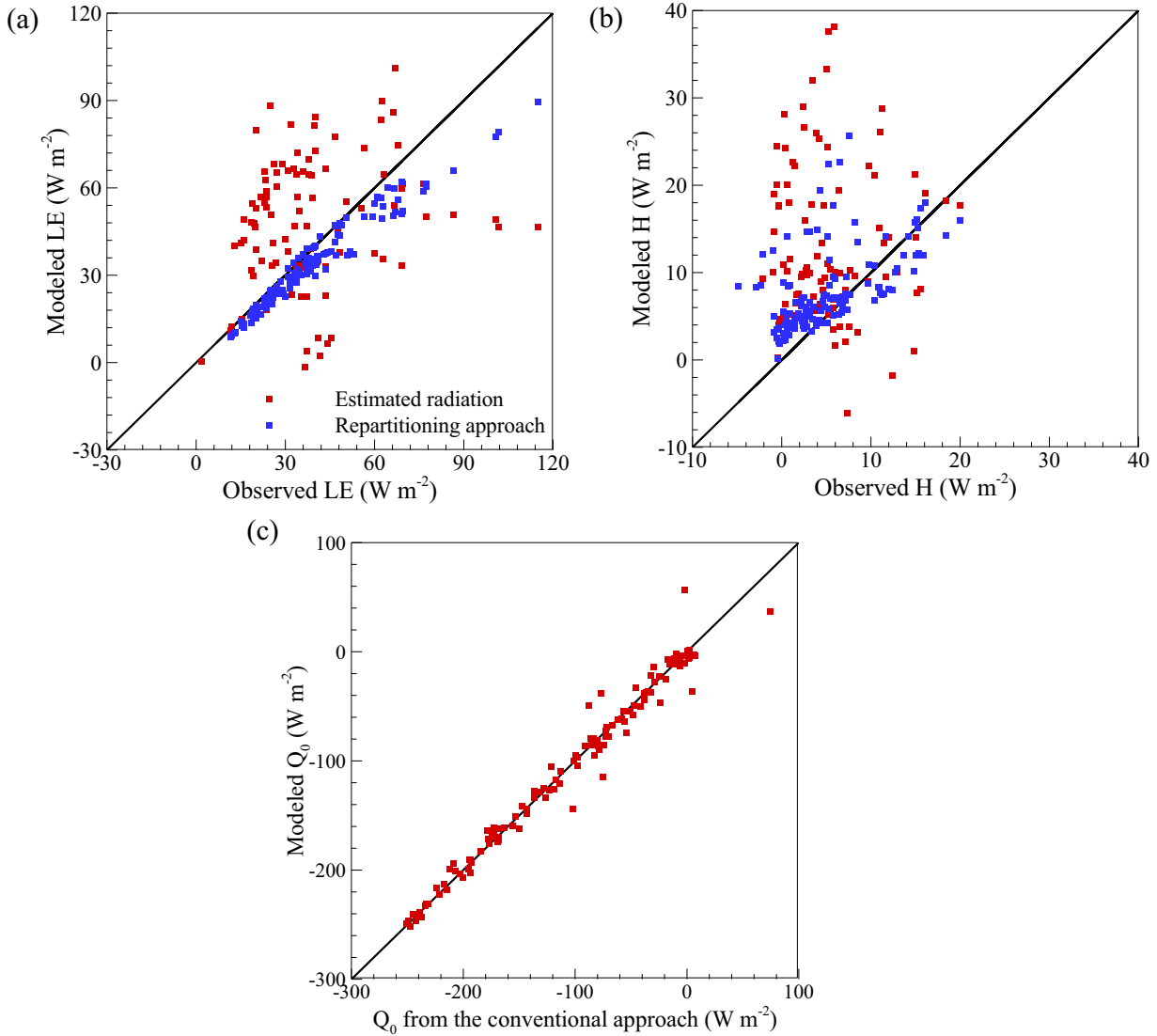


Fig. 6. Scatter plots of (a) predicted LE versus observation, (b) predicted H versus observation, and (c) predicted Q_0 from proposed method versus that from the conventional approach for 1 September–17 October 2006.

$$\begin{aligned}
 Q_0 = & \frac{I_{wsi}}{\sqrt{\pi}} \int_0^t \frac{\partial T_s(\tau)}{\partial \tau} \frac{d\tau}{\sqrt{t-\tau}} - \sum_j \mu_j \eta_j \sqrt{\kappa/\pi} \int_0^t \frac{R_s^n(\tau) d\tau}{\sqrt{t-\tau}} \\
 & + \int_0^t \sum_j \left[\mu_j^2 \eta_j \kappa e^{\mu_j^2 \kappa (t-\tau)} \operatorname{erfc}(\mu_j \sqrt{\kappa(t-\tau)}) \right] R_s^n(\tau) d\tau
 \end{aligned} \quad (23)$$

where $I_{wsi} = \sqrt{\rho_w c_w \lambda}$ is the thermal inertia parameter of water (Wang et al. 2014), ρ_w and c_w denote the density and specific heat of water. Once Q_0 is obtained, the MEP model can predict turbulent heat fluxes by distributing available energy at the surface ($R_s^n - Q_0$) based on the relative efficiency between H and LE in Eq. 22. Note that the MEP model only requires R_s^n , R_1^n , and T_s as inputs to estimate the surface energy budgets.

Model predictions by the proposed and the MEP methods are shown in Fig. 7. Predicted surface heat fluxes from both methods are in good agreement. A negative Q_0 value implies transport of thermal energy from water to the atmosphere. This confirms the finding in previous study that shortwave radiation absorption within the water layer close to the surface is an important energy source of the turbulent heat fluxes (Wang et al. 2014). Compared against observed turbulent fluxes and Q_0 from the conventional approach, the MEP model has RMSEs of about 25, 39, and 36 $W m^{-2}$ for H, LE, and Q_0 , respectively. These results indicate that the method proposed in this study has a slightly better overall performance than the MEP model, when driven by the accurate measurement of available energy, in predicting water surface

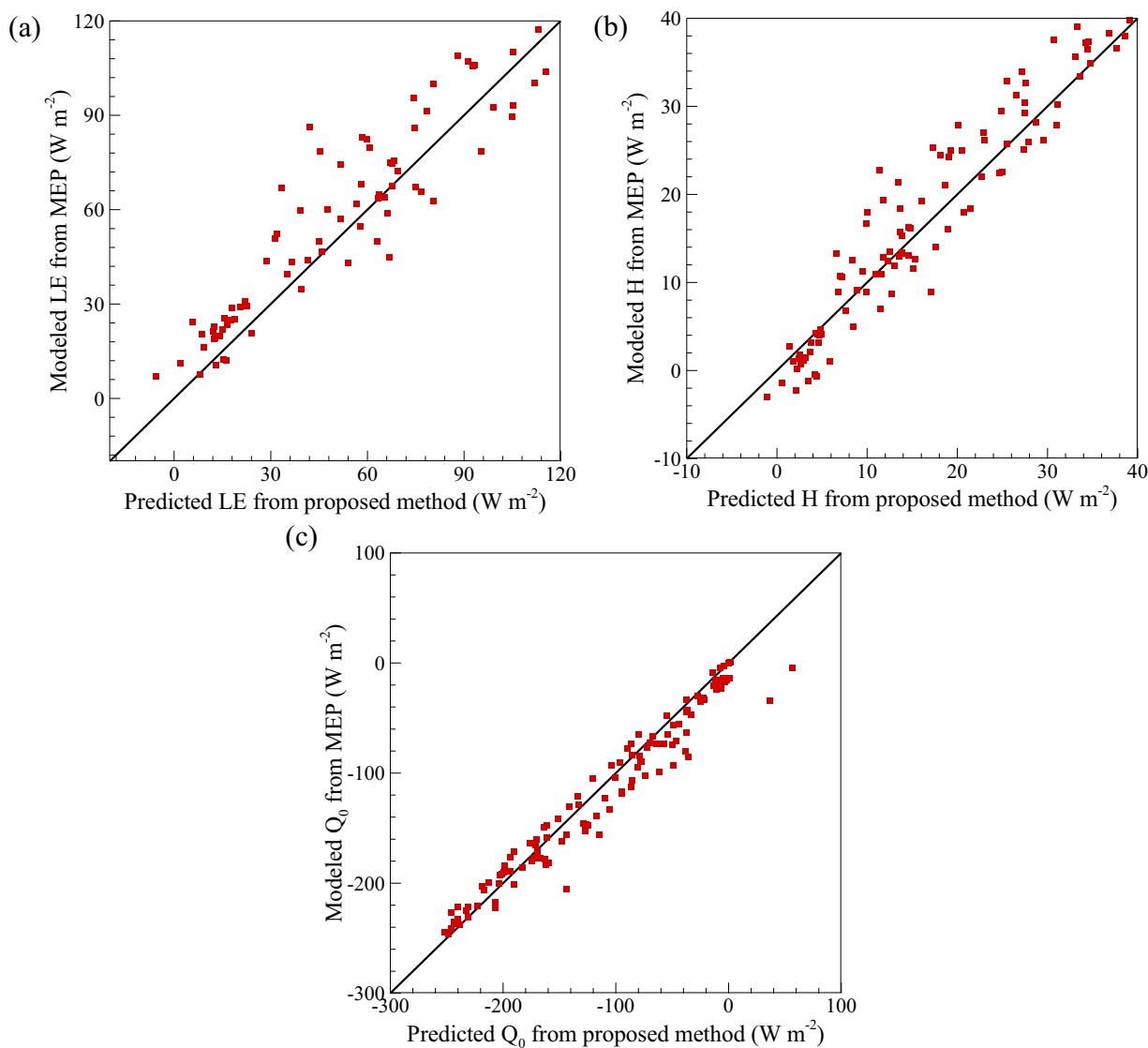


Fig. 7. Comparison of predicted (a) LE, (b) H, and (c) Q_0 from the MEP model and the proposed method for 1 September–17 October 2006.

energy balance over the study site. This finding is consistent with simulation results over land surface in previous study (Wang et al. 2014; Yang and Wang 2014).

Concluding remarks

In this study, we developed a new physically based scheme to estimate the surface energy components over water surface by combining the linear stability analysis and the Green's function approach. The underlying mechanism is that subsurface thermal mass in the mixed layer implicitly contains the signal of surface temperature evolution, which regulates the partitioning of solar energy at the surface. Capable of predicting all dissipative surface energy budgets, the method only requires the net longwave and shortwave radiative fluxes and temperature measurement at a single depth in the mixed

layer, and is thus highly suitable for large-scale applications. Performance of the proposed method is strongly affected by estimation of turbulent thermal diffusivity, which carries the information of meteorological and limnological conditions. Without explicitly using wind speed or temperature/moisture gradient, the method substantially reduces the uncertainty and potential error associated with meteorological measurements. Using the estimated κ from in situ measurements, results show that the model is able to reconstruct water temperature profile from a single-depth measurement reasonably well. With an accurate measurement of available energy at the water surface, predicted H and LE from the linear stability analysis method are in reasonable agreement with experimental observations. In addition, results of comparison with the MEP model illustrate that the proposed method is of better accuracy over the study site.

Though results from the proposed method are promising, there are a few limitations that need to be addressed in future studies. The contribution of aerodynamic conditions in parameterizing turbulent heat fluxes is not accounted in this study. This simplification underestimates the influence of aerodynamic conditions on surface energy partitioning, and may lead to considerable bias under strong wind condition. A uniform and time-invariant thermal diffusivity in vertical direction is assumed in this study based on previous data analysis (Vercauteren et al. 2011). This particular value is not expected to be universal, and the homogeneity and time-invariance assumptions might not hold in oceans or seas where mixing in the water body can fluctuate significantly more than in a lake. Though our simulation in this study does not strictly account for temporally varied κ , we recommend time and site-specific determination of turbulent thermal diffusivity, especially for study areas and periods where meteorological and limnological conditions change vastly. Another limitation is that model performance is evaluated with a limited data set of field measurements over a lake. Further tests of the proposed method over water surfaces with different fetch sizes (and over oceans and seas) and hydroclimatic conditions are needed, particularly when the turbulent diffusivity in the water is different from the typical lake value we use here. Nevertheless, the method proposed in this study offers a novel and physically based tool to predict water surface energy partitioning with a minimal set of information. With enhanced representation of water–atmosphere interaction, the method has potential applications for water ecosystems and oceanographic study, especially at large scales.

References

- Batani, S., and D. Entekhabi. 2012. Relative efficiency of land surface energy balance components. *Water Resour. Res.* **48**: W04510. doi: [10.1029/2011WR011357](https://doi.org/10.1029/2011WR011357)
- Best, M. J., and others. 2011. The Joint UK Land Environment Simulator (JULES), model description—Part 1: Energy and water fluxes. *Geosci. Model Dev.* **4**: 677–699. doi: [10.5194/gmd-4-677-2011](https://doi.org/10.5194/gmd-4-677-2011)
- Cole, K. D., J. V. Beck, A. Haji-Sheikh, and B. Litkouhi. 2010. *Heat conduction using Green's functions*, 2nd ed. Taylor and Francis.
- Crawford, T. M., and C. E. Duchon. 1999. An improved parameterization for estimating effective atmospheric emissivity for use in calculating daytime downwelling longwave radiation. *J. Appl. Meteorol.* **38**: 474–480. doi: [10.1175/1520-0450\(1999\)038<0474:AIPFEE>2.0.CO;2](https://doi.org/10.1175/1520-0450(1999)038<0474:AIPFEE>2.0.CO;2)
- Defant, A. 1961. *Physical oceanography*, v 1. Pergamon.
- Dewar, R. C. 2005. Maximum entropy production and the fluctuation theorem. *J. Phys. A: Math. Gen.* **38**: L371. doi: [10.1088/0305-4470/38/21/L01](https://doi.org/10.1088/0305-4470/38/21/L01)
- Fairall, C. W., E. F. Bradley, J. S. Godfrey, G. A. Wick, J. B. Edson, and G. S. Young. 1996. Cool-skin and warm-layer effects on sea surface temperature. *J. Geophys. Res.* **101**: 1295–1308. doi: [10.1029/95JC03205](https://doi.org/10.1029/95JC03205)
- Fee, E. J., R. E. Hecky, S. E. M. Kasian, and D. R. Cruikshank. 1996. Effects of lake size, water clarity, and climatic variability on mixing depths in Canadian Shield lakes. *Limnol. Oceanogr.* **41**: 912–920. doi: [10.4319/lo.1996.41.5.0912](https://doi.org/10.4319/lo.1996.41.5.0912)
- Granger, R. J., and N. Hedstrom. 2011. Modelling hourly rates of evaporation from small lakes. *Hydrol. Earth Syst. Sci.* **15**: 267–277. doi: [10.5194/hess-15-267-2011](https://doi.org/10.5194/hess-15-267-2011)
- Henderson-Sellers, A., P. Irannejad, K. Mcguffie., and A. Pitman, 2003. Predicting land-surface climates-better skill or moving targets? *Geophys. Res. Lett.* **30**: 1777. doi: [10.1029/2003GL017387](https://doi.org/10.1029/2003GL017387)
- Jerlov, N. G. 1976. *Marine optics*. Elsevier.
- Kiehl, J., and K. E. Trenberth. 1997. Earth's annual global mean energy budget. *Bull. Am. Meteorol. Soc.* **78**: 197–208. doi: [10.1175/15200477\(1997\)078<0197:EAGMEB>2.0.CO;2](https://doi.org/10.1175/15200477(1997)078<0197:EAGMEB>2.0.CO;2)
- Large, W. G., and S. Pond. 1982. Sensible and latent heat flux measurements over the ocean. *J. Phys. Oceanogr.* **12**: 464–482. doi: [10.1175/1520-0485\(1982\)012<0464:SALHF M>2.0.CO;2](https://doi.org/10.1175/1520-0485(1982)012<0464:SALHF M>2.0.CO;2)
- Leuning, R., E. Van Gorsel, W. J. Massman, and P. R. Isaac. 2012. Reflections on the surface energy imbalance problem. *Agric. For. Meteorol.* **156**: 65–74. doi: [10.1016/j.agrformet.2011.12.002](https://doi.org/10.1016/j.agrformet.2011.12.002)
- Liang, X., D. P. Lettenmaier, E. F. Wood, and S. J. Burges. 1994. A simple hydrologically based model of land surface water and energy fluxes for general circulation models. *J. Geophys. Res. Atmos.* **99**: 14415–14428. doi: [10.1029/94JD00483](https://doi.org/10.1029/94JD00483)
- Liebenthal, C., B. Huwe, and T. Foken. 2005. Sensitivity analysis for two ground heat flux calculation approaches. *Agric. For. Meteorol.* **132**: 253–262. doi: [10.1016/j.agrformet.2005.08.001](https://doi.org/10.1016/j.agrformet.2005.08.001)
- Morton, F. I. 1983. Operational estimates of lake evaporation. *J. Hydrol.* **66**: 77–100. doi: [10.1016/0022-1694\(83\)90178-6](https://doi.org/10.1016/0022-1694(83)90178-6)
- Mote, P., and A. O'Neill [eds.]. 2000. *Numerical modeling of the global atmosphere in the climate system*. Springer Science & Business Media.
- Niu, G. Y., and others. 2011. The community Noah land surface model with multiparameterization options (Noah-MP): 1. Model description and evaluation with local-scale measurements. *J. Geophys. Res.: Atmos.* **116**: D12109. doi: [10.1029/2010JD015139](https://doi.org/10.1029/2010JD015139)
- Oleson, K. W., and others. 2010. Technical description of version 4.0 of the Community Land Model (CLM). NCAR Tech. Note, NCAR/TN-478+STR266. Natl. Cent. Atmos. Res., Boulder, CO.

- Paulson, C., and J. Simpson. 1981. The temperature difference across the cool skin of the ocean. *J. Geophys. Res.* **86**: 11044–11054. doi: [10.1029/JC086iC11p11044](https://doi.org/10.1029/JC086iC11p11044)
- Rees, W. G., and S. P. James. 1992. Angular variation of the infrared emissivity of ice and water surfaces. *Int. J. Remote Sens.* **13**: 2873–2886. doi: [10.1080/01431169208904088](https://doi.org/10.1080/01431169208904088)
- Satterlund, D. R. 1979. An improved equation for estimating long-wave radiation from the atmosphere. *Water Resour. Res.* **15**: 1649–1650. doi: [10.1029/WR015i006p01649](https://doi.org/10.1029/WR015i006p01649)
- Stensrud, D. J. 2009. *Parameterization schemes: Keys to understanding numerical weather prediction models*. Cambridge University Press.
- Vercauteren, N., E. Bou-Zeid, M. B. Parlange, U. Lemmin, H. Huwald, J. Selker, and C. Meneveau. 2008. Subgrid-scale dynamics of water vapour, heat, and momentum over a lake. *Boundary-Layer Meteorol.* **128**: 205–228. doi: [10.1007/s10546-008-9287-9](https://doi.org/10.1007/s10546-008-9287-9)
- Vercauteren, N., E. Bou-Zeid, H. Huwald, M. B. Parlange, and W. Brutsaert. 2009. Estimation of wet surface evaporation from sensible heat flux measurements. *Water Resour. Res.* **45**: W06424. doi: [10.1029/2008WR007544](https://doi.org/10.1029/2008WR007544)
- Vercauteren, N., H. Huwald, E. Bou-Zeid, J. S. Selker, U. Lemmin, M. B. Parlange, and I. Lunati. 2011. Evolution of superficial lake water temperature profile under diurnal radiative forcing. *Water Resour. Res.* **47**: W09522. doi: [10.1029/2011WR010529](https://doi.org/10.1029/2011WR010529)
- Wallace, J. M., and P. V. Hobbs. 2006. *Atmospheric science: An introductory survey*. Academic Press.
- Wang, J., and R. L. Bras. 2009. A model of surface heat fluxes based on the theory of maximum entropy production. *Water Resour. Res.* **45**: W11422. doi: [10.1029/2009WR007900](https://doi.org/10.1029/2009WR007900)
- Wang, J., and R. L. Bras. 2011. A model of evapotranspiration based on the theory of maximum entropy production. *Water Resour. Res.* **47**: W03521. doi: [10.1029/2010WR009392](https://doi.org/10.1029/2010WR009392)
- Wang, J., R. L. Bras, V. Nieves, and Y. Deng. 2014. A model of energy budgets over water, snow, and ice surfaces. *J. Geophys. Res.: Atmos.* **119**: 6034–6051. doi: [10.1002/2013JD021150](https://doi.org/10.1002/2013JD021150)
- Wang, Z.-H. 2012. Reconstruction of soil thermal field from a single depth measurement. *J. Hydrol.* **464**: 541–549. doi: [10.1016/j.jhydrol.2012.07.047](https://doi.org/10.1016/j.jhydrol.2012.07.047)
- Wang, Z.-H., S. K. Au, and K. H. Tan. 2005. Heat transfer analysis using a Green's function approach for uniformly insulated steel members subjected to fire. *Eng. Struct.* **27**: 1551–1562. doi: [10.1016/j.engstruct.2005.05.005](https://doi.org/10.1016/j.engstruct.2005.05.005)
- Wang, Z.-H., and E. Bou-Zeid. 2012. A novel approach for the estimation of soil ground heat flux. *Agric. For. Meteorol.* **154**: 214–221. doi: [10.1016/j.agrformet.2011.12.001](https://doi.org/10.1016/j.agrformet.2011.12.001)
- Wüest, A., and A. Lorke. 2003. Small-scale hydrodynamics in lakes. *Annu. Rev. Fluid Mech.* **35**: 373–412. doi: [10.1146/annurev.fluid.35.101101.161220](https://doi.org/10.1146/annurev.fluid.35.101101.161220)
- Yang, J., Z. H. Wang, and T. Lee. 2013. Relative efficiency of surface energy partitioning over different land covers. *Brit. J. Environ. Clim. Change* **3**: 86–102.
- Yang, J., and Z. H. Wang. 2014. Land surface energy partitioning revisited: A novel approach based on single depth soil measurement. *Geophys. Res. Lett.* **41**: 8348–8358. doi: [10.1002/2014GL062041](https://doi.org/10.1002/2014GL062041)

Acknowledgments

This work is supported by the National Science Foundation under grant CBET-1435881 and Army Research Office under grants W911NF-15-1-0003 and W911NG-16-1-0045, and support from the Swiss Science Foundation and the Canadian NSERC program. Nikki Vercauteren received funding by the Deutsche Forschungsgemeinschaft (DFG) through grant number VE 933/2-1. Comments from the reviewers that helped to improve the manuscript are gratefully acknowledged.

Conflict of Interest

None declared.

Submitted 11 January 2016

Revised 29 April 2016; 16 June 2016

Accepted 24 June 2016

Associate editor: Francisco Rueda